Journal of Environmental Radioactivity 140 (2015) 130–140

Contents lists available at ScienceDirect

Journal of Environmental Radioactivity

journal homepage: www.elsevier.com/locate/jenvrad

Development of a neural network approach to characterise ^{226}Ra contamination at legacy sites using gamma-ray spectra taken from boreholes

Adam Varley [a, *], Andrew Tyler [a], Leslie Smith [b], Paul Dale [c]

[a] Department of Biological and Environmental Sciences, University of Stirling, Stirling FK9 4LA, UK
[b] Department of Computing Science and Mathematics, University of Stirling, Stirling FK9 4LA, UK
[c] Scottish Environmental Protection Agency, Radioactive Substances, Strathallan House, Castle Business Park, Stirling FK9 4TZ, UK

ARTICLE INFO

Article history:
Received 1 September 2014
Received in revised form
11 November 2014
Accepted 13 November 2014
Available online 29 November 2014

Keywords:
Borehole gammaspectroscopy
Radium contamination
Monte Carlo
Neural networks

ABSTRACT

There are a large number of sites across the UK and the rest of the world that are known to be contaminated with ^{226}Ra owing to historical industrial and military activities. At some sites, where there is a realistic risk of contact with the general public there is a demand for proficient risk assessments to be undertaken. One of the governing factors that influence such assessments is the geometric nature of contamination particularly if hazardous high activity point sources are present. Often this type of radioactive particle is encountered at depths beyond the capabilities of surface gamma-ray techniques and so intrusive borehole methods provide a more suitable approach. However, reliable spectral processing methods to investigate the properties of the waste for this type of measurement have yet to be developed since a number of issues must first be confronted including: representative calibration spectra, variations in background activity and counting uncertainty. Here a novel method is proposed to tackle this issue based upon the interrogation of characteristic Monte Carlo calibration spectra using a combination of Principal Component Analysis and Artificial Neural Networks. The technique demonstrated that it could reliably distinguish spectra that contained contributions from point sources from those of background or dissociated contamination (homogenously distributed). The potential of the method was demonstrated by interpretation of borehole spectra collected at the Dalgety Bay headland, Fife, Scotland. Predictions concurred with intrusive surveys despite the realisation of relatively large uncertainties on activity and depth estimates. To reduce this uncertainty, a larger background sample and better spatial coverage of cores were required, alongside a higher volume better resolution detector.

1. Introduction

1.1. Origin and regulation of radium contaminated land

At the start of 20th century, radium was being used for a multitude of purposes, including medicines, confectionaries and what would prove to its most beneficial use: a seemingly unbroken light source known as “Undark” (Kathren, 1998). Since these early explorations, not only has our understanding improved into the radioactive emissions released by radium and its decay series but also the detrimental mechanisms with which they interact with living tissue (Rundo, 1993; Paschoa, 1998). In the United Kingdom (UK), many redundant radium artefacts are now classified and controlled as low or intermediate level (HMSO, 1996).

Although the majority of radium production ended in the UK by the 1930's, radium salts were still imported for medical, industrial and military purposes into the 1960's (Tyler et al., 2013). In the absence of contemporary legislation, considerable quantities of highly radioactive radium waste were discarded by means of burial (Harvie, 1999). Only in 1960 was the use, keeping and disposal of radioactive sources controlled by statute through the Radioactive Substances Act 1960 and later the Radioactive Substances Act 1993 (HMSO, 1996). Examples of these legacy burial sites have also been identified in other parts of Europe and North America (Adams, 1993; Landa, 1993; Adsley et al., 2004).

It has been conservatively estimated that in the UK alone there are between 150 and 250 Radium Contaminated Legacy Sites (RCLS), but the number could be closer to 1000 (DECC, 2012).

* Corresponding author.
E-mail address: a.l.varley@stir.ac.uk (A. Varley).

http://dx.doi.org/10.1016/j.jenvrad.2014.11.011
0265-931X/

Considering the possible extent of contamination and the risk to society they pose, legislation has now been passed in UK allowing environmental regulatory agencies to identify, assess and, if needs be, designate radioactively contaminated land (Tyler et al., 2013).

1.2. Characterisation of radium contamination

Following the potential identification of any land as being contaminated with radium, the land has to be accurately characterised providing a foundation for subsequent dose calculations and risk assessments. This will determine whether actions are required in terms of remediation. Estimates of the source's activity, burial depth and lateral extent must be provided. Furthermore, knowledge of the localised extent of the source can be instrumental in proposed remediation strategies. Localised extent can be defined by source geometries where: the contamination can be considered more of a point source (in extreme cases referred to as a "hot" particle) or dissociated (or more appropriately an extended homogenous source). This will have implications on exposure pathways, transport processes, received dose and ultimately risk. In general, a point source (PS) is considered to be more hazardous, since human contact may result in a much higher dose than extended homogenous source (EHS) of similar activity. In the scenario where the risk a PS poses is considered too high, it should either be removed and disposed of or isolated to prevent human exposure (Dale et al., 2008). However, areas of contamination cannot always be categorised as singular PS or EHS. Often, many PS of similar activity (usually low activity) can be identified, either attributed to a number of small radioactive items or larger items mechanically broken up (Patton et al., 2013). This eventuality can be thought of as a Heterogeneous Source (HS), but separating HS from EHS via non-invasive methods can be very challenging. The aim of this work is to characterise highly radioactive PS.

1.3. Detection of radium contamination

For the most part, *in situ*, mobile and airborne gamma-spectrometry are the workhorses for large scale radioactive contamination land characterisation as alternative analytical methods tend to be expensive and time consuming, and can often be unrepresentative (Aage et al., 1999; Guillot, 2001; IAEA, 2003; Tyler, 2008; Kock et al., 2012). The majority of this research has been focussed on ^{137}Cs detection for extended sources (Tyler et al., 1996; Boson et al., 2009; Carrazana González et al., 2012) and "hot" particle detection (Maučec et al., 2004a; Davies et al., 2007; Tyler et al., 2010). Up to now, however, very few researchers have focussed their efforts on characterising RCLS (Thummerer and Jacob, 1998; Adsley et al., 2004; Haddad et al., 2014). Yet, with an increasing awareness of the potential number of contaminated sites in existence, it is essential that efficient methods be developed for their rapid and accurate characterising.

At any RCLS, the principal contaminant tends to be ^{226}Ra and its progeny which is a reflection of the long half-life of ^{226}Ra and its persistence in the environmental. Direct gamma-spectrometry of ^{226}Ra in the environment is challenging as it only has one relatively weak low energy gamma ray from which to infer its activity (186 keV). Subsequently its daughter products (^{214}Bi and ^{214}Pb) are conventionally used as a proxy measure. However, this can be inherently problematic as secular equilibrium is not always encountered as a result of ^{222}Rn emanation. To address this issue, many studies assume the fulfilment of equilibrium introducing systematic uncertainty to any ^{226}Ra activity estimations (Thummerer and Jacob, 1998; Hendriks et al., 2001). Before reliable approximations of depth, activity and localised distribution of ^{226}Ra can be made, four inherent confounding factors must first be respected:

- If the photon flux received by a detector is low, gaining acceptable counting uncertainty on the measurement can be impractical.
- ^{226}Ra and daughter products form part of the ^{238}U decay series where concentration variations can vary considerably over the scale of meters.
- As a source is buried an exponential decrease in unscattered photons is observed with the vast majority of photons that reach the detector being scattered.
- At energies below 150 keV, photons, although numerous, tend to undergo photoelectric absorption making the composition of the geological matrix an important control on photon flux (Tyler, 1999, 2008). Backscattered photons (<250 keV) can also be challenging to interpret.

These factors, acting in combination, influence the confidence with which a source in the presence of a typically heterogeneous background radiation field can be resolved. Moreover, once a source has been identified, considerable uncertainties relating to its localised extent and activity can remain. It is for these reasons *in situ* and mobile gamma-spectroscopy of ^{226}Ra PS, below observed activity thresholds (<70 MBq), is considered impractical below depths of about 70 cm. This is because the majority of the source signal, particularly the intense low energy peaks below 609 keV, is enveloped by background noise with increasing source depth. Measurements beyond this depth must therefore be addressed with borehole measurements (Wilson and Conaway, 1991; Meisner et al., 1995; Adsley et al., 2004; Bugai et al., 2005).

1.4. The borehole measurement

Borehole measurements are customarily taken as a depth series, when the detector is lowered into the borehole. Ensuing spectra can then provide knowledge into layers of contamination if sufficient spatial coverage is performed to validate extrapolation (Adsley et al., 2004; Bugai et al., 2005). Otherwise, the shape and magnitude of standalone spectra offer insight into localised source arrangements (Giles and Dooley, 1998). Subtle changes occurring within the spectrum's overall shape, suggestive of alterations in source geometry and activity, could potentially correspond to the presence of contamination. Identifying such changes is invaluable in the search for hazardous "hot" particles in close proximity of the borehole (Wilson et al., 1997). For a detailed review of borehole measurements refer to Kobr et al. (2005).

The source geometries, Extended Homogeneous source (EHS), Point Source (PS) and for completeness Heterogeneous Source (HS) are illustrated alongside the detector in a borehole geometry (Fig. 1). First consider a PS, where D is the mass thickness of shielding (g cm^{-2}) and θ is its angle perpendicular to the axis of detector. The measure mass thickness was preferred over Euclidean distance, since it takes into account the amount of shielding, related to the density of soil, which can significantly vary with depth and lateral position (Tyler, 2008). Secondly, an EHS can be described by E_d indicating its vertical depth with its midpoint at the centre of the detector's active volume. For completeness the final geometry HS, is a differing number of PS at variable D from the detector; this eventuality will be considered by this study as EHS.

Exploring the parameters, E_d and D, as spectral shape drivers is the fundamental aim of this study. Nevertheless, other parameters known to influence spectral shape, although not the primary focus in this study, such as soil density and the constituent that make up

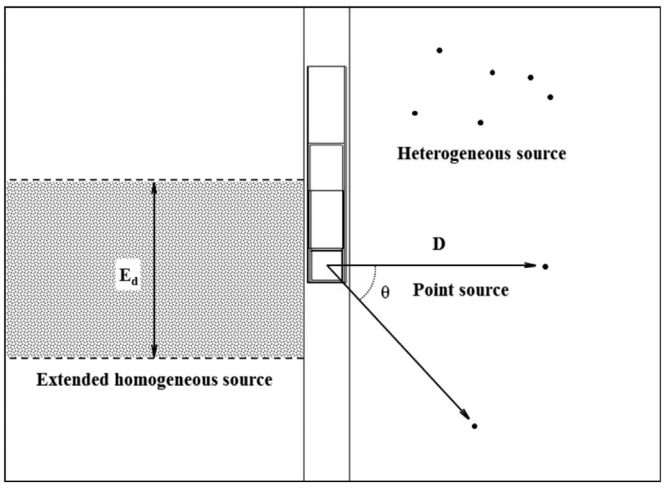

Fig. 1. Cross-section of the detector in the borehole including the source geometries of interest: Extended homogeneous source, Point source and Heterogeneous source.

background must be added by way of assessing the uncertainties that will be introduced to any conclusions of activity and geometry.

1.5. Spectral processing

Without contamination present, changes in the shape and magnitude of borehole spectra will almost exclusively be due to deviations in background activity (^{40}K, ^{238}U series and ^{232}Th series) and shielding influences brought about by changes in soil density and composition (Fig. 2). If a site is contaminated, it is the fundamental goal of a surveyor to differentiate between these benign background fluctuations in spectral shape and those initiated by the presence of ^{226}Ra contamination, particularly presented from a PS at great distance from the detector. However, establishing information from spectra that have relatively sparse counts contributed from contamination can be very difficult. Additionally, in most cases there is likely to be a continuum of activities, shielding arrangements and source geometries within contaminated sites resulting in a similar continuum of detector response (Wei et al., 2010). Therefore, characterisation methods applied for ^{226}Ra contamination must be robust enough to cope with fluctuations in background but at the same time be sensitive enough to provide reliable estimates of activity and depth (Fig. 2).

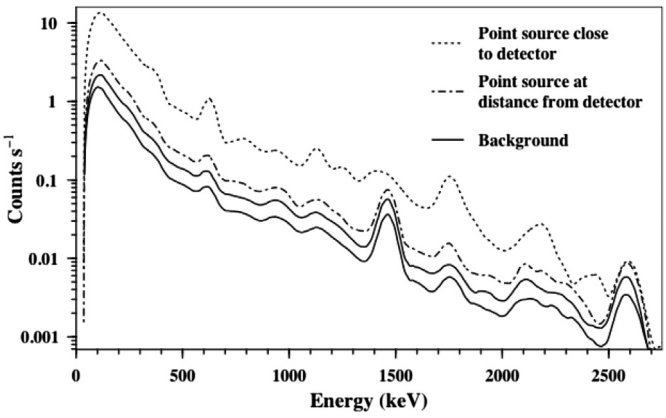

Fig. 2. Changes in spectral shape brought about by the introduction of a point source at different distances from the detector. Note the similarity in signal presented by a point source at distance and typical background spectra.

The important spectral unfolding process, providing insight into relative spectral contributions, is not an instructive one and firstly requires extensive knowledge of the individual detectors response to known source geometries which must be provided by a robust calibration procedure. Complications often arise when trying to account for, by analytical calibration methods, the extensive environmental scenarios that can lead to spectral changes particularly for extended sources. Monte Carlo simulations (MCS) present a more suitable way to account for environmental variables such as density, soil composition and source geometry (Forster et al., 1990; Hendriks et al., 2002).

Once a dynamic calibration dataset has been collected, relating it to field observations can be problematic. A commonly applied method of interpreting the signal from a detector is gross counting. This approach provides only a relative measure of the total flux of photons (or dose rate) and little information of source distribution since energy discrimination is not performed (Adsley et al., 2004). A more adequate method that relies on the differential attenuation of two or more of the numerous intense full energy peaks, ^{214}Bi (609, 1120, 1764 and 2240 keV) and to a lesser extent ^{214}Pb (295, 351 keV), can be used to establish the amount of shielding between the source and detector (Miller et al., 1994; Trnková et al., 2010; Haddad et al., 2014). However, the method can be severely hindered by the need to strip out background counts and poor counting statistics, often peaks in low-resolution detectors cannot be formed. Alternatively, a more sophisticated approach, coined "Full Spectral Analysis", can be applied. This method attempts to add linear combinations of calibration data to the vast majority of the channels of a field spectrum by a Poisson weighted least squares fitting procedure (Hendriks et al., 2001; Maučec et al., 2004b) or Non-negative least squares algorithm (Caciolli et al., 2012; Guastaldi et al., 2013) followed by a χ^2 goodness of fit test. Unfortunately, this method requires sufficiently low counting uncertainty across the spectrum to reliably fit individual spectral contributions; a scenario that is not always obtainable in the field. Moreover, fitting calibration spectra for this application may become complicated by the fact there is a continuum of contamination and multiple source distribution under investigation.

It is well understood that gamma-spectrometry data taken from the environment will contain similarities in spectral shape, or, more precisely, channels will regularly exhibit correlation from one measurement to next. This will be predominantly due to background contributions to each individual spectrum (Fig. 2). Difficulties can arise when trying to apply conventional statistical approaches to a dataset when this redundant cross-channel correlation has not been taken into consideration (Fagan et al., 2012). Principal Component Analysis (PCA) is a method commonly used to explore the underlying structure of a multivariate dataset and was employed in this study to contend with variation in background.

The mathematical derivation (Hotelling, 1933; Chatfield and Collins, 1980) and in depth discussions regarding the different implementation of PCA (Hovgaard, 1997; Runkle, 2006) can be found in the literature. Essentially, PCA multiplies the spectral matrix by its, mean-centred, singular value decomposed matrix producing a set of uncorrelated variables. Generally the first few sets of loadings associated with their corresponding Principal components (PCs) of the decomposed matrix can then be considered as representative of the source signal and can be set aside for further statistical analysis (Im et al., 2007). Another convenient outcome of the PCA process is that the number of dimensions is significantly reduced as lower order elements are generally discounted as noise contributions.

The second step utilised the pattern recognition capabilities of a Neural Network (NN) to classify source geometry and approximate activity, mass depth (D) and vertical depth (E_d) from higher order

PCs. The basic design framework of neural networks (NNs) is analogous to the human brain and they have been used to solve many complex non-linear problems across a variety of fields including gamma-ray spectroscopy (Yoshida et al., 2002; Dragovic et al., 2005; Dragović et al., 2006). They have even been used to map counts directly to activity and source burial depth (Wei et al., 2010).

An NN is composed of a number of processing units known as nodes that are, by convention, separated into three distinct layers: the input, hidden and output. The input layer is a collection of the nodes defining the explanatory variables of the problem. The hidden layer can in fact be made up of one or more layers and the output layer, contains the desired response variables. The hidden layer provides the NN the ability to learn non-linear transformations. Each node has its own weight set, with the weights defining the strength of the connections between neurons in adjacent layers (Yoshida et al., 2002). The weights are established during a training phase where the error between predicted outputs and desired output of the specified training set is minimised in an iterative fashion (Medhat, 2012). For a detailed review of the workings of NNs refer to Gurney (2003).

The aims of this study were:

- Investigate whether PS and EHS can be distinguished from each other in the borehole geometry.
- Apply optimised method to an RCLS providing estimates of activity and source distribution.

2. Materials and methods

2.1. Field site: headland dataset

Dalgety bay, Fife, Scotland, is a former military site where wartime and post-wartime activities have led to specific areas of the site becoming associated with ^{226}Ra contamination (Tyler et al., 2013). Following the sites decommissioning a new town was built on the area (also called Dalgety Bay) with a Sailing club located on the on the west coast where much of the radium contamination was believed to be deposited (Fig. 3). Public access along the coast provide the opportunity for the general public to come into contact with potentially harmful sources via either direct contact, ingestion or inhalation (Dale et al., 2008; Tyler et al., 2013).

An intrusive survey was undertaken and borehole measurements were obtained from an area on the headland around the sailing club previously suspected of having contamination at depths beyond the capabilities of conventional surface measurements (Tyler et al., 2011). Cores were not necessarily concentrated around the highest surface signal as indicated by the *in situ* survey (Fig. 3), as surface sources and contaminated material were recovered from many of these locations. Another feature is a large proportion of the cores were situated either on the edge of the headland and around the main sailing clubhouse (middle top) as re-deposition of contamination by sea erosion and contact with the general public were the primary concerns of the original survey.

Due to the heterogeneous composition of the soil matrix, a relatively small diameter auger (60 mm diameter) was used since penetration into the contaminated site with an auger with a larger diameter was likely to have been unviable. A total 30 augered holes with varying depths (0.2–1.6 m) were taken over identified hotspots and a 51 × 51 mm Sodium iodide (NaI:Tl) detector, encased in plastic tubing, was lowered into each hole. Spectra with 1024 channels representing an energy range of 20–3000 keV were recorded using Ortec's Maestro software, at 0.1 m depth intervals for at least 600 s to attain reasonable counting statistics. This dataset is referred to as the "Headland dataset" (HD) for the remaining discussions.

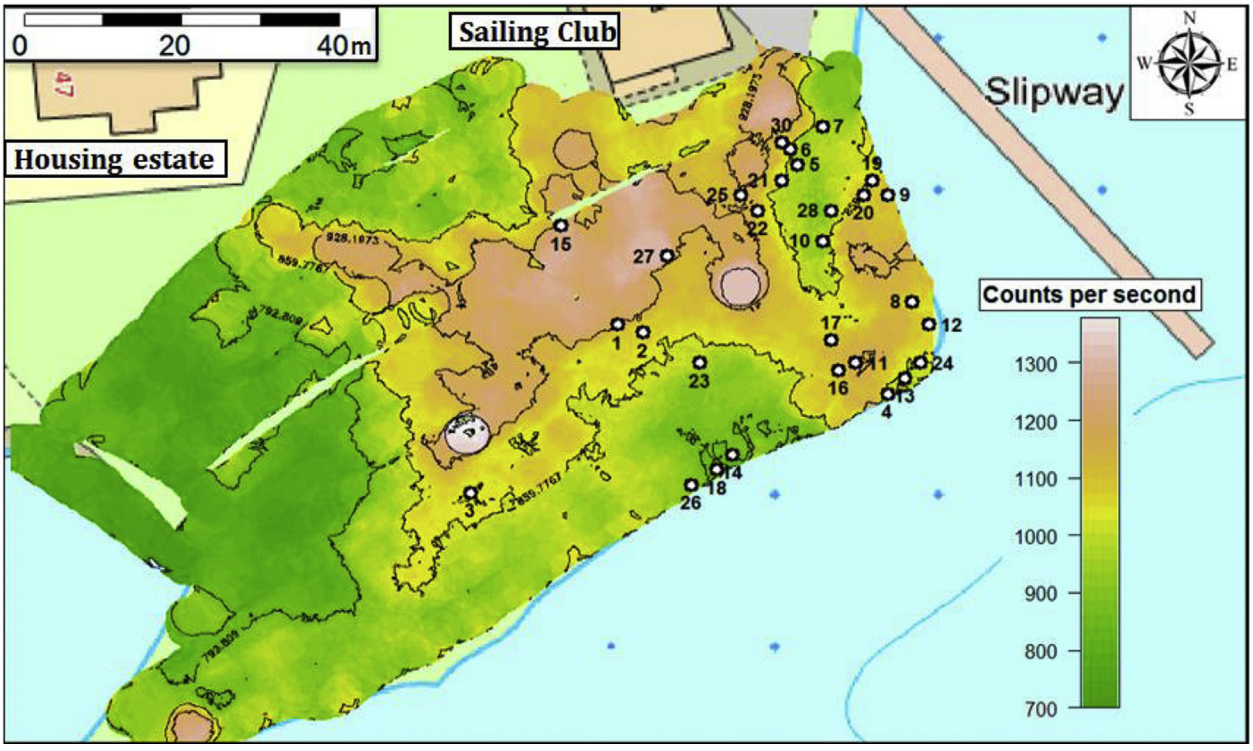

Fig. 3. Maps of the headland with gross counts using a 76 × 76 mm handheld Lanthanum bromide detector overlaid. The surface was interpolated using ordinary Kriging. Locations and numbers of boreholes have been included.

2.2. Monte Carlo

Monte Carlo codes offer a robust alternative to either labour intensive and expensive experimental calibration or mathematically cumbersome deterministic approaches (Stromswold, 1995; Maučec et al., 2009). For example, acquiring representative laboratory spectra can be hindered by the need to strip out the laboratory background which can vary slightly over long acquisition times due to problems of radon exhalation. This can, for example, introduce significant error when using relatively weak calibration sources at large distances. Field calibration although more characteristic of the background at the HD site presents practical problems of burying the source and being confident of its distance from the detector and the exact amount of shielding (i.e. density of soil) between the source and the detector. Numerous studies, facing similar challenging calibration situations, have opted for and successfully applied Monte Carlo Simulations (MCS) to a variety of environmental measurements (Maučec et al., 2004a; Allyson and Sanderson, 1998). The code used in this study was Monte Carlo N-Particle eXtented (MCNPX) (Briesmeister, 1993).

2.2.1. MCNPX optimisation

The simulations used in this study only retained key features of the NaI:Tl detector, such as the active volume, aluminium outer canning and protective plastic piping, since this was found to accurately account for scattering within the real detector. Beck's "standard" soil composition was used for all simulations since the actual soil composition was not known (Beck et al., 1972). Decay data was obtained from the National Nuclear Data Centre (2013) and only emissions with relative abundance of 1% were used in the simulations for all radionuclides.

Although MCS possess clear advantages over conventional calibration procedures, there is a major drawback, in that the time it can take to obtain acceptable uncertainty on average particle fluxes can be unfeasible (Likar et al., 2004). This is because each particle must be tracked from birth until death where during its lifetime a large number of irrelevant interactions take place consuming computer time. Although there are a number of accessible variance reduction techniques available to use in MCNPX, for example population control methods, if the modeller does not exercise considerable precaution, bias can be introduced to the final tally results (Allyson, 1994; Serov et al., 1998).

This study used a more straightforward procedure. Firstly Multigroup/adjoint calculations were utilised, to estimate the vertical and lateral extent needed to accurately reconstruct an entire environmental spectrum from extended sources; commonly described as the detector's Field Of View (De Groot et al., 2009). In short, this special treatment of photons sees the problem effectively reversed, with photons starting in the detector and gaining energy until a cut off of 2614 keV (the highest environmental photon energy) was reached (Maučec et al., 2004b). Covering the density range that was likely to be present at the site (1.1–1.8 g cm^{-2}), it was found that the soil thickness needed to accurately recreate a borehole spectrum was 0.5 m above and below the detector 0.55 m parallel to the borehole. After this, a method outlined by Hendriks et al. (2002) was used involving only electrons in close proximity to the detector being tracked and sampling bremsstrahlung energies for those that were terminated outside this proximity. This was accomplished by the use of surface source write/surface source read cards within MCNPX.

2.2.2. Benchmark experiments

To validate the code defining the geometry, materials and response of the detector a benchmark investigation to a known source geometry and activity was undertaken. At the time of measurement, no borehole calibration facility was available. A set of flat concrete pads doped with ^{40}K, ^{238}U and ^{232}Th geared more towards *in situ* and airborne calibration were used instead. The MCNPX Gaussian Energy Broadening (GEB) feature was used to reconstruct the broadened peaks generated by the detector.

Spectra from the concrete calibration pads and MCS are in good agreement (Fig. 4). The ^{232}Th and ^{238}U pads were reproduced well. Minor discrepancies were found in the simulated Compton continuum of the ^{40}K pad where it was overestimated compared to the pad, this was noted by another study (Hendriks et al., 2002). This is likely to be caused by the different positions of pads at the calibration facility resulting in incomplete removal of background contribution by the background pad.

2.3. Spectral compilation

Before any spectral interpretation of the HD could be performed, enough data spanning the range of environmental variables thought to be present at the site had to be generated so as to embody the relevant spectral shapes. Additionally, establishing the overall spread of the spectral population obtained by sensibly varying model parameters provides uncertainty estimates for any conclusions made about the parent source distribution. This step is also essential prior to training an NN as extrapolations outside of datasets are known to be very unreliable (Moreira et al., 2010).

This procedure could not be performed purely in MCNPX because of time constraints, because on average it took approximately 4 h for each simulation to attain acceptable statistical uncertainty even with optimisation. Instead a resampling procedure of a discrete range of MCNPX generated spectra, encompassing only changes in source geometry and density variation, was undertaken. This permitted more straightforward parameters, such as spectral drift and relative spectral contribution (or activity) to be sampled and adjusted afterwards allowing a larger and more robust spectral dataset to be produced. The rest of this section details this methodology.

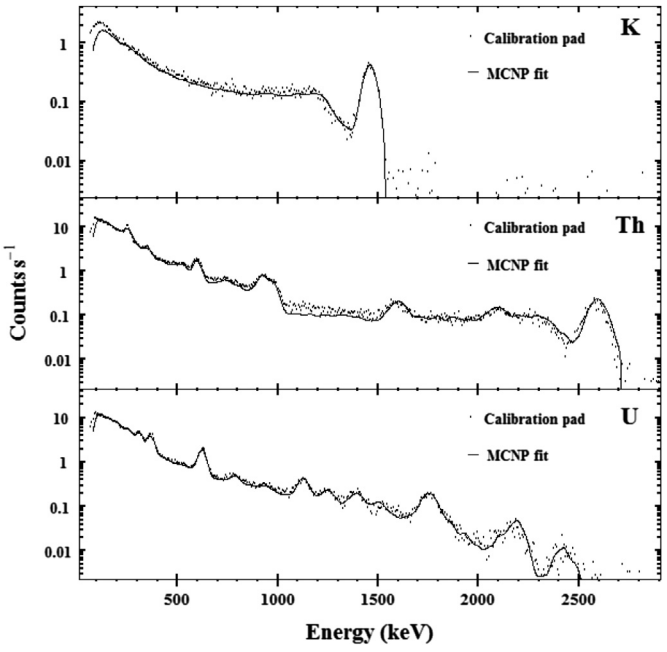

Fig. 4. Benchmark experiment results showing MCNPX fitted data (lines) to calibration pad (Potassium, Thorium and Uranium) data (dots).

All source and background spectra were simulated within MCNPX covering representative densities from 1.1 to 1.8 g cm^{-3} with intervals of 0.1 g cm^{-3}, typical of the densities range found within the cores taken at the site. Energies below 300 keV were disregarded to avoid systematic uncertainties associated with variations in geological matrix (Hendriks et al., 2002; Caciolli et al., 2012). Fig. 5A demonstrates good agreement in count rate below 300 keV between MCS and field spectra "28 90 cm" although this was not the case for spectra obtained. Good agreement in spectral shape was nonetheless maintained above 300 keV for the remaining measurements.

A base count rate of ~24 counts per second (for the energy range above 300 keV) was used as the mode count rate of a lognormal distribution established from a background core with minimum and maximum count rates of 13 and 65 counts s^{-1} respectively. Whilst the probability of reaching background count rates of 65 counts s^{-1} was considered extremely unlikely at Dalgety bay headland, it was thought best to take a conservative approach with the little spatial coverage of background data that was available. Although, this would raise the limit of detection and uncertainty on final activity and depth predictions the spectral shape recognition capabilities of the proposed method was anticipated to negate such fluctuations. Relative contributions from each of the natural decay series were found to be reasonable well correlated within background cores demonstrated by Pearson's linear correlation coefficient above 0.8. This deviation was accounted for within the model.

The background dataset was then spiked using selected simulated source spectra of corresponding density and a randomly sampled activity. Spectral drift was introduced into each spectrum by sampling a Gaussian distribution with a standard deviation of 3 keV (at 1461 keV) typically found within the temperature and magnetic field variations within the environment for the detector in question. The MCS were recorded to a much higher statistical accuracy, typically >95%, to form the "Training dataset (Fig. 5). Field results were known to have a greater noise element due to the limited counting time and detector volume (Minty and Hovgaard, 2002). Accordingly, Poisson noise was introduced into individual bins depending on a sampled count rate (>600 s). The addition of noise established the "Validation dataset" and was considered to be more representative of the error structure of the HD (Fig. 5A).

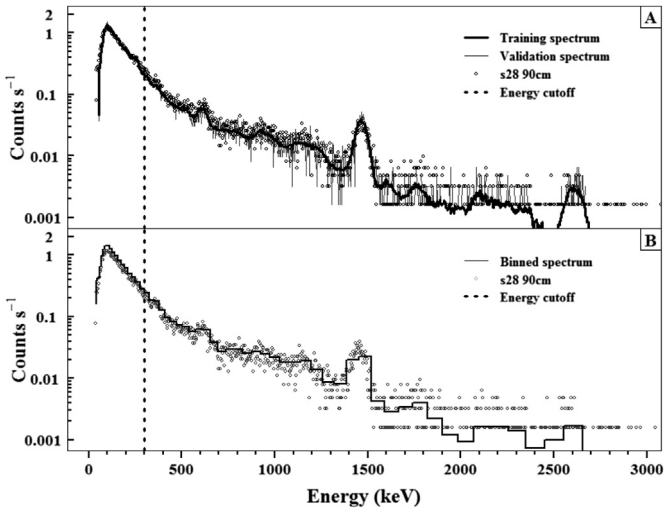

Fig. 5. A) Example simulated background alongside a field measurement taken from core 28 at 90 cm. Note that the "Training spectrum" is far more statistically defined than either the Poisson noise induced "Validation spectrum" and "s28 90 cm". B) Full Width at Half Maximum binning intervals used on all spectra.

Clearly using over 1000 energy bins presents a large relative variation within individual bins from one spectrum to the next, particularly as counts become sparse at higher energies. To reduce this surplus noise without too much loss of energy distinction, the energy range 300–2918 keV was irregularly binned according to the estimated Full Width at Half Maximum established using the same Gaussian Energy Broadening model fit implemented in MCNPX (Briesmeister, 1993). Higher energy spectral features can be observed more easily as the sparse nature of counts is diminished, for instance the ^{208}Th (2614 keV) and ^{214}Bi (1764 keV) peaks (Fig. 5B). Conversely, at low energy where the FWHM is lower spectral structure is not lost, observe the low energy ^{214}Bi (609 keV) can still be observed.

All relevant sample data: source Activity (A), PS depth (D) and vertical depth (E_d) was recorded for individual spectra. PCA was then carried out on the combined simulated dataset and HD to allow comparison. All steps mentioned were carried out using the base features in the software package R (R Development Core Team, 2012).

2.4. Neural network: training procedure

To optimise the performance of the NN and ensure that the trained network was learning general patterns within the problem rather than adapting to the training data itself, three separate data sets were produced: the training set, a test set and cross validation set (Dragovic et al., 2005). All datasets were mean centred and scaled relative to the variance. Initially, each NN was trained and tested with statistically defined MCNP spectra (spectral drift was added to ensure SCs remained similar). The essential stage of cross validation was performed using data with Poisson noise introduced "Validation dataset" which was known to be more characteristic of the noisy HD (Fig. 5). The transformation used in the hidden layer was a sigmoidal function and the algorithm used to train the network was resilient backpropogation (Riedmiller and Braun, 1993). The R package RSNNS was used to construct and train all NNs (Bergmeir and Benítez, 2012).

The architecture of an NN may be different from one problem to the next depending on the problem's level of complexity. It was discovered early on to reach the optimised level of performance for this problem it was better to divide the procedure into three separate networks since this eliminated crosstalk effects between the output neurons specifying the activity and depth parameters of an EHS and a PS. The first NN's purpose was to classify spectra into one of the three classes: background, EHS or PS. The final networks were then used to make estimates regarding activity (kBq or Bq kg^{-1}), burial depth (g cm^{-2}) and lateral extent (cm). Crucially, they were only trained and tested with spectra that were identified by the classification network. To ensure that the correct architecture for each network was selected an exhaustive search was conducted to: establish the number of PCs to use in the input layer, the number of hidden nodes and hidden layers, and the number of learning epochs. Decisions made regarding the design of the network were based around minimising the error within the validation dataset. This was checked again using confusion matrices for classification results (Zell et al., 1993) and R^2 values for any regression results produced by the EHS and PS networks (Moreira et al., 2010). Between 1000 and 2000 training data were found to adequately train all the networks. Test and validation sets were 30% of the training set.

Uncertainty on regression results was estimated by resampling the predicted output values 50 times using the original background parameters. These values were then fed back into the original network alongside the training data and the standard deviation of the injected values was used as the uncertainty. Caution was taken

not to bias the latent variables used by PCA with introduction of new values, since this would have influenced final NN outputs. To avoid this eventuality the procedure was looped where error spectra values were introduced into the original dataset one at a time.

3. Results and discussion

3.1. Analysis of principal components

90% of the total variance within the dataset was explained by the first 5 principal components, which suggests the latter PCs possess largely noise elements. Visual analysis of the PC 1 and PC 2 loadings demonstrates the merit of the PCA transform: at this early stage of analysis point source effective depth is being separated within PC space with shielding thickness variation (Fig. 6). This is confirmed by the shallow point source depth (larger lighter points towards the bottom of the plot), in contrast to deeper sources (smaller darker points) towards the top left of the plot. Interestingly, distance from the background pack (Crosses) would appear to infer activity.

Arguably conventional separation techniques, such as a Mahalanobis distance metric could be used to delineate a boundary between source and background (Runkle, 2006). Moreover, a linear regression between PC1 and PC2 could be performed to establish a relationship with depth and activity (Adams et al., 2012). However, a number of problems may be encountered using these approaches. Firstly, separation via parametric methods (i.e. Mahalanobis distance) invariably contains a distribution-based assumption, normally a multivariate Gaussian distribution, to define separation limits from the background dataset. This assumption is often not correct leading to misclassification. Secondly and most crucially, separation of the extended source population, encompassed by the black lines in Fig. 6, from point sources in the intermediate range (2–20 g cm^{-2}) is not possible through a linear regression technique, and this is of particular importance since a large proportion of the HD lie within this region. Furthermore analyses of lower order PCs, using a similar approach, becomes increasingly challenging. This suggests that to reliably separate extended sources from point sources more information from lower order PCs is needed but the relationship is likely to be non-linear. To confront these issues three separate NN were used to establish structure within the PC loadings.

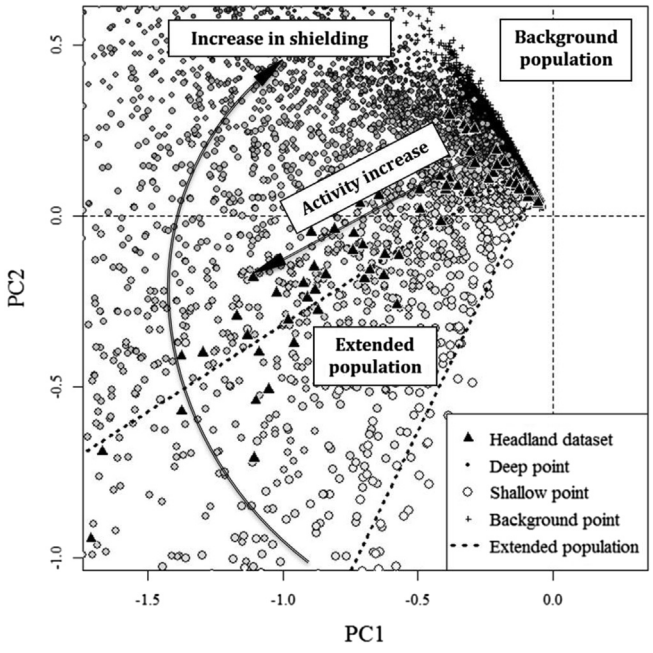

Fig. 6. Plot of Principal components 1 and 2 loadings. Background spectra (Black crosses) are tightly clustered in the top right of the plot. Differing sizes and shades of circular points indicate varying thicknesses of shielding and greater distance from the background pack infers greater activity. The extended population are bound by the black dotted lines. The headland dataset are represented by black triangles.

3.2. Classification network

The first NN was used to classify spectra into one of the three classes. It was established by using the first 5 PCs, a hidden layer with 16 neurons and 1500 learning epochs gave the smallest Relative Mean Squared Error (RMSE) on the cross validation dataset (~15%) in the case of the classification network. It must be noted at this early stage, throughout this work comparatively large errors were encountered on output neurons for the cross validation sets due to the noise introduced during spectral compilation (Section 2.3). Another outcome was that networks were trained using relatively few iterations compared to other studies (Moreira et al., 2010; Dragović et al., 2006).

The final output of the classification NN (CNN) was decided by the "Winner takes all" approach and the overall performance assessed by calculating the misclassification rate (Zell et al., 1993). The highest misclassification was witnessed on the background results (10.2%) due to the low activities used at large depths for both PS and EHS within the cross validation set. It was decided to include these levels in order to attain detection limits. Generally PS's were classified well above a certain threshold, dependent on the activity and depth, representing the minimum detectable activity (MDA) where source becomes misclassified as background as source count contributions became negligible (Fig. 7A). EHS were also characterised well, however misclassified shallow depth PS (5–20 g cm^{-2}) can be seen distributed along on the MDA boundary (<10 Bq kg^{-1}) (Fig. 7B). As expected as the extent depth (E_d) becomes less and the overall volume of the contaminated layer is reduced, leading to less source contributions, the MDA increases to about 30 Bq kg^{-1}. The most significant case of misclassification can be seen subtended within PS results between 5 and 20 g cm^{-2} and below 10 kBq in which a 37% classification rate was found (Fig. 7A). This implies the two populations must still significantly overlap within PC space and the NN struggles to separate as too few source counts were contributed to the already noisy background spectra. The second reason is that the spectral shape, regardless of noise, in these specific geometries is too similar, using only energies above 300 keV, for the NN to separate. It is likely a combination of the two has led to this misclassification uncertainty. If energies below 300 keV could be sufficiently characterised these populations could be more effectively resolved. This however presents a real challenge.

This method presents a real improvement in comparison to a traditional parametric approach where this degree of separation would not be possible (Fig. 6). Consideration must also be drawn to the areas of significant misclassification, for example, PS's under 10 kBq at depths below 20 g cm^{-2}. This circumstance does not pose a great risk compared to more active PS which are more than likely be classified correctly (Fig. 7A).

3.3. Point and extended neural networks

Quantification of activity and depth (both D and E_d) was performed using two final NNs: Point (PNN) and Extended (ENN). Interestingly both required only 3 PCs as inputs to accurately estimate depth, but it was soon recognised that to stabilise activity estimates a fourth input neuron specifying total counts should be

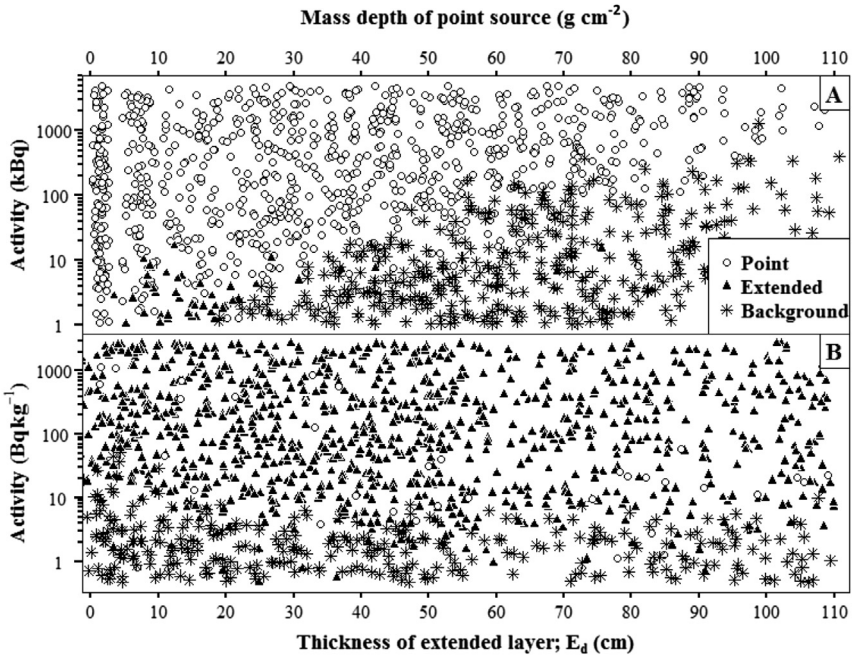

Fig. 7. Classification Neural Network output for A) Point source and B) Extended source. Discrete depths have been jittered slightly to give a better sense of population density. The legend in plot A conceals largely background-misclassified points.

included. The number of hidden neurons and the size of training set needed to accurately map the problem in both NN cases were roughly similar to the CNN (Table 1). Again, a relatively small number of iterations were required to attain RMSE minima on the cross validation datasets (<25 000) and it was documented during training that both networks were found to diverge rapidly after convergence: indicative of sudden overtraining (Medhat, 2012).

During the training of preliminary networks it was established by limiting the maximum activity of training and test sets to realistic environmental constraints, for example PS (<5 MBq) and EHS (<3 kBq kg^{-1}), uncertainties on more probable lower activity sources could be reduced. Such activity constraints are well within activities found during intrusive surveys of Dalgety bay headland (Patton et al., 2013).

Drawing attention to accuracy of the models, the overall ability of both NN's to generalise a relationship was good for activity estimates. This is supported by high R^2 values (PNN = 0.955 (<0.001) and ENN = 0.937 (<0.001)) for both NN's. PS depth prediction was additionally very good (R^2 value of 0.942 (<0.001)). Predictions made by the ENN for vertical depth (E_d) were not as reliable (R^2 value of 0.670(<0.001)). This suggests that very subtle changes in spectral shape occur as the thickness of the layer contamination is varied, and these cannot be identified as easily as the change in spectral shape of PS with variable depth. This is understandable since the majority of photons that reach the detector will have originated from areas close to the detector. Thus with increasing thickness of contamination relatively less signal is received due to the inverse square law. Consequentially, accurate measurements of E_d are unlikely and predictions made by the ENN for this parameter should be treated with caution.

Table 1
Input parameters and R^2 values (and accompanying p-values in brackets) produced for the cross validation dataset for Point Neural Network and Extended Neural Network.

Neural network	Iteration number	Number of neurons in hidden layer	Size of training set	R^2 value	
				Depth	Activity
Point	25,000	16	1000	0.942 (<0.001)	0.910 (<0.001)
Extended	8000	10	2000	0.670 (<0.001)	0.965 (<0.001)

3.4. Analysis of the headland dataset

To demonstrate the capacity of the method, analysis of two cores from the HD is included (Fig. 8). Firstly, confidence within the ENN predictions is provided by comparing the similarity in shape of the total count rate (Fig. 8A.1 and Fig. 8B.1) and activity estimates (Bq kg^{-1}) (Fig. 8A.2 and Fig. 8B.2) with core depth for both the cores. Interestingly, the majority of the HD measurements (~70%) that were identified as having contamination were predicted to be EHS. This outcome supports general intrusive findings at the headland where the majority of contaminated material is well distributed ash and clinker from the burning of radioactive artefacts (Patton et al., 2013).

An important finding was the identification of a relatively thick (~90 cm) elevated activity extended layer (357 ± 69 Bq kg^{-1}) at 130 cm within "s21" (Fig. 8B.2). This coincides with a large spike in total count rate (Fig. 8B.1). In the original survey this was disputed to be a point source due to the Gaussian nature of the total count rate increase within the depth series. Even with further analysis using the differential peak method the source signal could not be classified. This scenario clearly demonstrates the value of the current approach.

The highest predicted extended activities (600–700 Bq kg^{-1}) were found in a relatively thin contaminated section of core "s7" at 160–180 cm (Fig. 8A.2). This area did not contribute the highest total count rate (>1000 counts per second) though; as seen in core "s21" (Fig. 8B.1). This highest count rate was caused by a thicker (95 ± 11 cm) less active (520 ± 85 Bq kg^{-1}) layer. This shows that using this technique can provide insight into the thickness of a layer meaning that more accurate estimations of activity can be made instead of assuming a completely distributed source. Another key feature that the CNN identified at core depths between 90 and

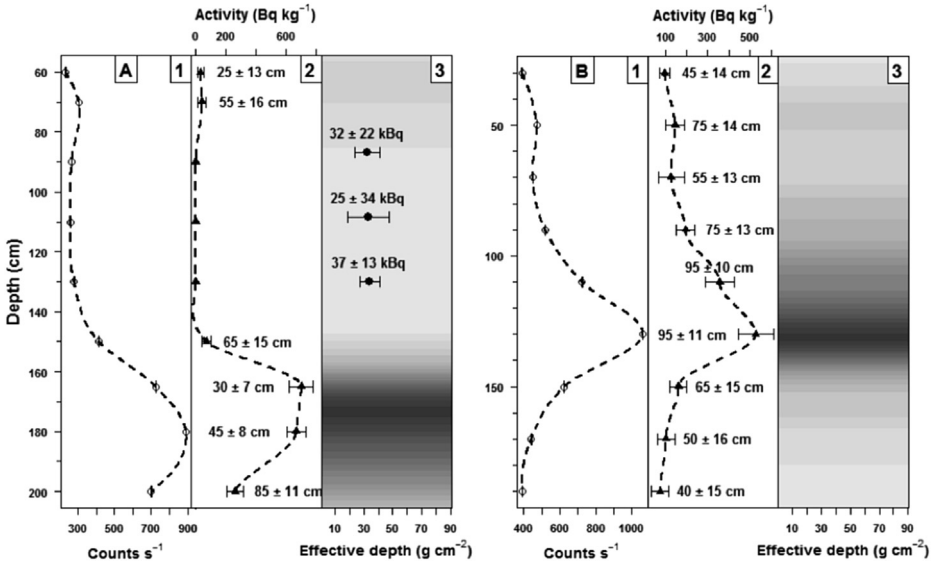

Fig. 8. Neural network results for cores "s7" (A) and "s21" (B) taken from the Headland dataset. Individual core results have been separated into three individual plots 1, 2 and 3. Plot 1 provides total count rate (20–3000 keV) as a function of depth (error bars are hidden behind points). Plot 2 gives Extended Neural Network predictions for activity (Bq kg^{-1}) on the *x* axis and vertical depth (cm) estimates are accompanying text values. Plot 3 offers a visual representation of the core with darker shading indicating higher activity homogeneous contamination (similar to plot B) and whether a point source is present and at what depth (*x* axis) and activity (accompanying text values) it occurs.

130 cm was the presence of PS's in between two extended layers (Fig. 8A.3). The PNN provided clarification that these sources were at relatively short distances away from the detector (~35 g cm^{-2}) and at low activities (~30 kBq). Although PS were identified by the network, the consistency of the activities and depth would suggest the detector is in a pocket of low contaminated soil with larger activities at greater distances from the detector. Algorithmic identification of this situation would be very challenging. This emphasises the importance of human interpretation. To verify this notion further cores would have to be taken. This scenario highlights a real limitation of the borehole measurement without substantial spatial coverage. Similar geometries that are beyond the scope of the technique to differentiate, and that would require further spatial coverage would be for example, localised areas of homogeneous contamination that are not distributed symmetrically around the borehole and measurements above or below an extended layer.

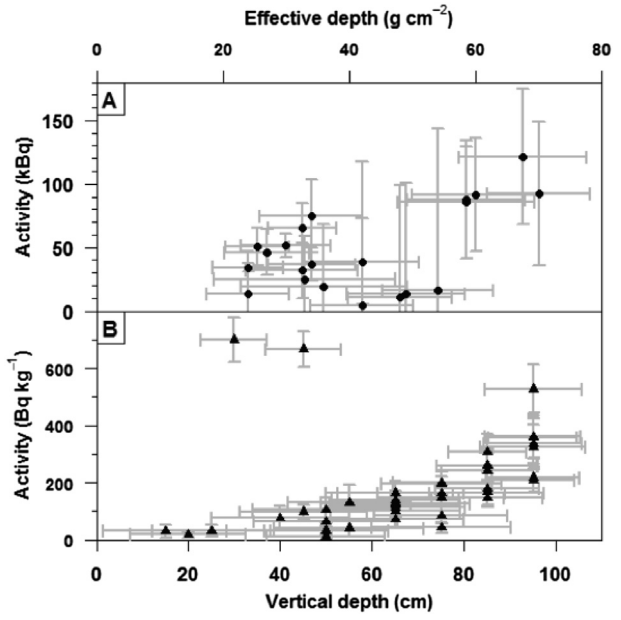

Fig. 9. Estimated uncertainties associated with Headland dataset source measurements A) Point Source and B) Extended Homogeneous Source.

Attention must be drawn to the errors associated with predictions of activity and depth from the NN's (Fig. 9). Standard deviations from both networks showed similar patterns, generally with increasing burial depth and decreasing activity the relative standard deviation increased. This is particularly prevalent with the point source estimations at effective depths of 30–40 g cm^{-2} and less than 20 kBq (Fig. 9A), and low activity (<100 Bq kg^{-1}) sections (<40 cm) of contamination (Fig. 9B), and this practically renders these readings unusable. This is understandable as source spectral shape would have become increasingly difficult to differentiate from background as source counts became too few.

Interestingly, the deepest and highest activity predictions for PS occurred at the base of two cores that were positioned close together, suggestive of high activity at depth. Without further boreholes to confirm this, the actual activities are challenging to deduce as they are so far away from the detector.

There are practical ways to alleviate some of the uncertainty associated with field results, indicated by the large error bars (Fig. 9). Firstly reduction in counting uncertainty across the energy range could be attained by using another detector. NaI(Tl) detectors have relatively low energy resolution and the size used in this survey was particularly small (51 × 51 mm). If a larger, higher resolution detector was used, such as a larger volume Lanthanum bromide, uncertainties could be reduced (Yongpeng and Bin, 2012).

Another way to reduce uncertainty would be to collect more background results to provide a better understanding of the background population. This study was limited by this fact resulting in a conservative estimate of background population being made. This would have would have invariably raised the limit of detection and introduced more uncertainty on final activity and depth predictions. Other than collecting further background cores at the site, cores could have also been drilled deeper beyond contamination (providing little stratification of background constituents was present), giving more reliable background estimates for individual cores. However, this was not possible at much of the site as hard rock restricted further augering.

4. Conclusions

^{226}Ra contamination at depths typically below 50 cm cannot be reliably measured using conventional surface gamma-ray measurements. Borehole gammaspectroscopy is used for the purpose of characterisation, where details of the geometric nature of contamination and activity estimates are vital if formal risk assessments are to be developed in order to protect the general public. Current methods of spectral processing, however, either do not have the ability to perform the task or prove unreliable.

An approach has been described based upon feature extraction using PCA, followed by NN's to relate key features of representative MCS to obtained field results. This method provided a reliable means to characterise the geometric nature of contamination, offer activity and depth estimates of point sources, and give insight into potential layers of homogeneous contamination. The potential of the technique was demonstrated by analysis of core data taken from Dalgety Bay Headland where prediction from the majority of cores suggested that contamination was mostly dissociated: supporting intrusive survey findings.

Nevertheless, limitations associated with the nature of the borehole measurement still remain and cannot realistically be solved unless adequate spatial coverage is performed, making some predictions very uncertain, particularly of PS at distance. The use of improved detector technology and better understanding of the background could, however, alleviate some of the estimated uncertainty associated with predictions from the method.

Acknowledgements

The authors would like to thank the Scottish Environmental Protection Agency and the Natural Environmental Research Council (NE/I018956/1) for funding the work, and the Dalgety Bay Sailing Club for allowing access onto the site. Additional thanks must be given to Mike Davies and Pete Burgess for useful suggestions.

References

Aage, H.K., Korsbech, U., Bargholz, K., Hovgaard, J., 1999. A new technique for processing airborne gamma ray spectrometry data for mapping low level contaminations. Appl. Radiat. Isotopes 51, 651–662.
Adams, A., 1993. The origin and early development of the Belgian radium industry. Environ. Int. 19, 491–501.
Adams, J.C., Joyce, M.J., Mellor, M., 2012. The advancement of a technique using principal component analysis for the non-intrusive depth profiling of radioactive contamination. Nucl. Sci. IEEE Trans. 59, 1448–1452.
Adsley, I., Davies, M., Murley, R., Pearman, I., Scirea, M., 2004. 3D GPS mapping of land contaminated with gamma-ray emitting radionuclides. Appl. Radiat. Isotopes 60, 579–582.
Allyson, J.D., 1994. Environmental Gamma-ray Spectrometry: Simulation of Absolute Calibration of In-situ and Airborne Spectrometers for Natural and Anthropogenic Sources. PhD thesis. Glasgow University, p. 274.
Allyson, J.D., Sanderson, D.C.W., 1998. Monte Carlo simulation of environmental airborne gamma-spectrometry. J. Environ. Radioact. 38, 259–282.
Beck, H., De Campo, J., Gogolak, C., 1972. In Situ Ge (Li) and Na (Tl) Gamma-ray Spectrometry. US Department of Energy, Environmental Measurements Laboratory, HASL-258, New York.
Bergmeir, C., Benítez, J.M., 2012. Neural networks in R using the Stuttgart neural network simulator: RSNNS. J. Stat. Softw. 46, 1–26.
Boson, J., Plamboeck, A.H., Ramebäck, H., Ågren, G., Johansson, L., 2009. Evaluation of Monte Carlo-based calibrations of HPGe detectors for in situ gamma-ray spectrometry. J. Environ. Radioact. 100, 935–940.
Briesmeister, J.F., 1993. MCNP-a General Monte Carlo N-particle Transport Code. LA-12625.
Bugai, D., Kashparov, V., Dewiere, L., Khomutinin, Y., Levchuk, S., Yoschenko, V., 2005. Characterization of subsurface geometry and radioactivity distribution in the trench containing Chernobyl clean-up wastes. Environ. Geol. 47, 869–881.
Caciolli, A., Baldoncini, M., Bezzon, G.P., Broggini, C., Buso, G.P., Callegari, I., et al., 2012. A new FSA approach for in situ γ ray spectroscopy. Sci. Total Environ. 414, 639–645.
Carrazana González, J., Cornejo Díaz, N., Jurado Vargas, M., 2012. Application of the Monte Carlo code DETEFF to efficiency calibrations for in situ gamma-ray spectrometry. Appl. Radiat. Isotopes 70, 868–871.
Chatfield, C., Collins, A.J., 1980. Principal Component Analysis. In Anonymous Introduction to Multivariate Analysis. Springer, pp. 57–81.
Dale, P., Robertson, I., Toner, M., 2008. Radioactive particles in dose assessments. J. Environ. Radioact. 99, 1589–1595.
Davies, M., McCulloch, G., Adsley, I., 2007. Experience of monitoring beaches for radioactive particles. J. Radiol. Prot. 27, A51.
De Groot, A., Van der Graaf, E., De Meijer, R., Maučec, M., 2009. Sensitivity of in-situ γ-ray spectra to soil density and water content. Nucl. Instrum. Methods Phys. Res. A Accel. Spectrom. Detect. Assoc. Equip. 600, 519–523.
DECC, 2012. Radioactive Contaminated Land Statutory Guidance Environmental Protection Act 1990: Part 11A. Contaminated Land. Department of Energy and Climate Change 2012.
Dragovic, S., Onjia, A., Stankovic, S., Anicin, I., Bacic, G., 2005. Artificial neural network modelling of uncertainty in gamma-ray spectrometry. Nucl. Instrum. Methods Phys. Res. A Accelerators Spectrom. Detect. Assoc. Equip. 540, 455–463.
Dragović, S., Onjia, A., Bačić, G., 2006. Simplex optimization of artificial neural networks for the prediction of minimum detectable activity in gamma-ray spectrometry. Nuclear Instrum. Methods Phys. Res. A Accelerators Spectrom. Detect. Assoc. Equip. 564, 308–314.
Fagan, D.K., Robinson, S.M., Runkle, R.C., 2012. Statistical methods applied to gamma-ray spectroscopy algorithms in nuclear security missions. Appl. Radiat. Isotopes 70, 2428–2439.
Forster, R., Little, R., Briesmeister, J., Hendricks, J., 1990. MCNP capabilities for nuclear well logging calculations. Nucl. Sci. IEEE Trans. 37, 1378–1385.
Giles, J., Dooley, K., 1998. High resolution gamma-spectroscopy well logging system. J. Radioanalytical Nucl. Chem. 233, 125b–130.
Guastaldi, E., Baldoncini, M., Bezzon, G., Broggini, C., Buso, G., Caciolli, A., et al., 2013. A multivariate spatial interpolation of airborne γ-ray data using the geological constraints. Remote Sens. Environ. 137, 1–11.
Guillot, L., 2001. Extraction of full absorption peaks in airborne gamma-spectrometry by filtering techniques coupled with a study of the derivatives. Comparison with the window method. J. Environ. Radioact. 53, 381–398.
Gurney, K., 2003. An Introduction to Neural Networks. CRC Press, p. 139.
Haddad, K., Al-Masri, M.S., Doubal, A.W., 2014. Determination of ^{226}Ra contamination depth in soil using the multiple photopeaks method. J. Environ. Radioact. 128, 33–37.
Harvie, D.I., 1999. The radium century. Endeavour 23, 100–105.
Hendriks, P., Limburg, J., De Meijer, R., 2001. Full-spectrum analysis of natural γ-ray spectra. J. Environ. Radioact. 53, 365–380.
Hendriks, P.H.G.M., Maučec, M., de Meijer, R.J., 2002. MCNP modelling of scintillation-detector γ-ray spectra from natural radionuclides. Appl. Radiat. Isotopes 57, 449–457.
HMSO, 1996. CM 2919 (1995) Review of Radioactive Waste Management Policy-final Conclusions.
Hotelling, H., 1933. Analysis of a complex of statistical variables into principal components. J. Educ. Psychol. 24, 417.
Hovgaard, J., 1997. Airborne Gamma-ray Spectroscopy. Airborne Gamma-ray Spectrometry.
IAEA, 2003. Guidelines for Radioelement Mapping Using Gamma Ray Spectrometry Data. Nuclear Fuel Cycle and Materials Section, International Atomic Energy Agency, p. 173.
Im, H., Lee, Y., Park, Y.J., Song, B.C., Cho, J., Kim, W., 2007. Noise reduction in prompt gamma spectra acquired in short times. Nucl. Instrum. Methods Phys. Res. A Accelerators Spectrom. Detect. Assoc. Equip. 574, 272–279.
Kathren, R.L., 1998. NORM sources and their origins. Appl. Radiat. Isotopes 49, 149–168.
Kobr, M., Mareš, S., Paillet, F., 2005. Geophysical well logging. In: Anonymous Hydrogeophysics. Springer, pp. 291–331.
Kock, P., Lanke, J., Samuelsson, C., 2012. A real-time statistical alarm method for mobile gamma spectrometry—Combining counts of pulses with spectral distribution of pulses. Nucl. Instrum. Methods Phys. Res. A Accel. Spectrom. Detect. Assoc. Equip. 681, 55–60.
Landa, E.R., 1993. A brief history of the American Radium Industry and its ties to the Scientific Community of its early twentieth century. Environ. Int. 19, 503–508.
Likar, A., Vidmar, T., Lipoglavšek, M., Omahen, G., 2004. Monte Carlo calculation of entire in situ gamma-ray spectra. J. Environ. Radioact. 72, 163–168.
Maučec, M., de Meijer, R.J., Rigollet, C., Hendriks, P.H.G.M., Jones, D.G., 2004a. Detection of radioactive particles offshore by γ-ray spectrometry Part I: Monte Carlo assessment of detection depth limits. Nucl. Instrum. Methods Phys. Res. A Accel. Spectrom. Detect. Assoc. Equip. 525, 593–609.
Maučec, M., de Meijer, R.J., van der Klis, M.M.I.P., Hendriks, P.H.G.M., Jones, D.G., 2004b. Detection of radioactive particles offshore by γ-ray spectrometry Part II: Monte Carlo assessment of acquisition times. Nucl. Instrum. Methods Phys. Res. A Accel. Spectrom. Detect. Assoc. Equip. 525, 610–622.
Maučec, M., Hendriks, P.H.G.M., Limburg, J., de Meijer, R.J., 2009. Determination of correction factors for borehole natural gamma-ray measurements by Monte Carlo simulations. Nucl. Instrum. Methods Phys. Res. A Accel. Spectrom. Detect. Assoc. Equip. 609, 194–204.
Medhat, M.E., 2012. Artificial intelligence methods applied for quantitative analysis of natural radioactive sources. Ann. Nucl. Energy 45, 73–79.
Meisner, J., Nicaise, W., Stromswold, D., 1995. CsI (Tl) with photodiodes for identifying subsurface radionuclide contamination. Nucl. Sci. IEEE Trans. 42, 288–291.
Miller, K.M., Shebell, P., Klemic, G.A., 1994. In-situ Gamma-Ray spectrometry for the measurement of uranium in surface soils. Health Phys. 67, 140–150.

Minty, B., Hovgaard, J., 2002. Reducing noise in gamma-ray spectrometry using spectral component analysis. Explor. Geophys. 33, 172–176.
Moreira, M.C.F., Conti, C.C., Schirru, R., 2010. A new NaI(Tl) four-detector layout for field contamination assessment using artificial neural networks and the Monte Carlo method for system calibration. Nucl. Instrum. Methods Phys. Res. A Accel. Spectrom. Detect. Assoc. Equip. 621, 302–309.
National Nuclear Data Center, 2013. Nuclear Datasheets.
Paschoa, A.S., 1998. Potential environmental and regulatory implications of naturally occurring radioactive materials (NORM). Appl. Radiat. Isotopes 49, 189–196.
Patton, N., Gemmill, J., Milne, J., 2013. Appropriate Person Report. Scottish Environmental Protection Agency.
R Development Core Team, 2012. R: a Language and Environment for Statistical Computing.
Riedmiller, M., Braun, H., 1993. A Direct Adaptive Method for Faster Backpropagation Learning: the RPROP Algorithm, pp. 586–591.
Rundo, J., 1993. History of the determination of radium in man since 1915. Environ. Int. 19, 425–438.
Runkle, R., 2006. Analysis of spectroscopic radiation portal monitor data using principal components analysis. IEEE Trans. Nucl. Sci. 53, 1418–1423.
Serov, I.V., John, T.M., Hoogenboom, J.E., 1998. A new effective Monte Carlo Midway coupling method in MCNP applied to a well logging problem. Appl. Radiat. Isotopes 49, 1737–1744.
Stromswold, D., 1995. Calibration facilites for borehole and surface environmental radiation measurements. J. Radioanal. Nucl. Chem. 194, 393–401.
Thummerer, S., Jacob, P., 1998. Determination of depth distributions of natural radionuclides with in situ gamma-ray spectrometry. Nucl. Instrum. Methods Phys. Res. A Accelerators Spectrom. Detect. Assoc. Equip. 416, 161–178.
Trnková, L., Trojek, T., Thinová, L., 2010. Gamma spectrometric measurements of depth-related radionuclide distribution in walls. Appl. Radiat. Isotopes 68, 832–835.
Tyler, A.N., 1999. Monitoring anthropogenic radioactivity in salt marsh environments through in situ gamma-ray spectrometry. J. Environ. Radioact. 45, 235–252.
Tyler, A.N., 2008. In Situ and Airborne Gamma-ray Spectrometry. Radioactivity in the Environment. Elsevier, pp. 407–448.
Tyler, A.N., Sanderson, D.C.W., Scott, E.M., Allyson, J.D., 1996. Accounting for spatial variability and fields of view in environmental gamma ray spectrometry. J. Environ. Radioact. 33, 213–235.
Tyler, A.N., Scott, E.M., Dale, P., Elliott, A.T., Wilkins, B.T., Boddy, K., et al., 2010. Reconstructing the abundance of Dounreay hot particles on an adjacent public beach in Northern Scotland. Sci. Total Environ. 408, 4495–4503.
Tyler, A.N., Ruffell, A., Dale, P., 2011. Dalgety Bay Headland Investigation (Prepared for Scottish Environmental Protection Agency).
Tyler, A., Dale, P., Copplestone, D., Bradley, S., Ewen, H., McGuire, C., et al., 2013. The radium legacy: contaminated land and the committed effective dose from the ingestion of radium contaminated materials. Environ. Int. 59, 449–455.
Wei, W., Du, Q., Younan, N.H., 2010. Particle swarm optimization based spectral transformation for radioactive material detection and classification. Comput. Intell. Meas. Syst. Appl. 1–6.
Wilson, R., Conaway, J., 1991. Simulations of a Spectral Gamma-ray Logging Tool Response to a Surface Source Distribution on the Borehole Wall. Los Alamos National Laboratory Publication, pp. 1118–1122.
Wilson, R.D., Koizumi, C.J., Meisner, J.E., Stromswold, D.C., 1997. Spectral Shape Analysis for Contaminant Logging at the Hanford Site. Los Alamos National Laboratory Publication, pp. 457–461.
Yongpeng, W., Bin, T., 2012. Monte-carlo simulation of response functions for natural gamma-rays in LaBr3 detector system with complex borehole configurations. Plasma Sci. Technol. 14, 481.
Yoshida, E., Shizuma, K., Endo, S., Oka, T., 2002. Application of neural networks for the analysis of gamma-ray spectra measured with a Ge spectrometer. Nucl. Instrum. Methods Phys. Res. A Accelerators Spectrom. Detect. Assoc. Equip. 484, 557–563.
Zell, A., Mache, N., Huebner, R., Mamier, G., Vogt, M., Herrmann, K., et al., 1993. SNNS-Stuttgart Neural Network Simulator, pp. 1–155.